Available online at www.sciencedirect.com
SCIENCE DIRECT®
Acta Materialia 52 (2004) 2279–2291
Acta MATERIALIA
www.actamat-journals.com

Effect of thermal history on the superplastic expansion of argon-filled pores in titanium: Part II modeling of kinetics

N.G.D. Murray [1], D.C. Dunand *

Department of Materials Science and Engineering, Northwestern University, 2220 Campus Drive, Evanston, IL 60208, USA

Received 7 November 2003; accepted 14 January 2004

Abstract

Metals can be foamed to ca. 50% porosity in the solid state by the creation of gas-pressurized pores within the metal, followed by expansion of these pores at elevated temperatures. We present here models for the time-dependence of pore expansion during solid-state foaming performed under isothermal conditions, where the metal deforms by creep, and under thermal cycling conditions, where superplasticity is an additional deformation mechanism. First, a continuum-mechanics model based on the creep expansion of a pressure vessel provides good quantitative agreement with experimental data of isothermal foaming of titanium, and qualitative trends for the case of foaming under thermal cycling conditions. Second, an axisymmetric finite-element model provides predictions very similar to those of the pressure-vessel model, indicating that stress-field overlap is unimportant when pores are equidistant. Numerical modeling shows that stress-field overlap increases foaming rate when pores are clustered, and also cause anisotropic pore growth. However, a bimodal distribution of pore size was found to have little effect on pore growth kinetics.

Keywords: Metals; Foams; Creep; Porosity; Transformation superplasticity

1. Introduction

In a companion paper [1], we presented an experimental study of foaming of titanium, utilizing solid-state expansion of argon pores at elevated temperatures; the argon-filled pores had been trapped within a commercially pure titanium (CP-Ti) matrix during hot-isostatic pressing of powders. At constant temperature, foaming occurs as the metallic matrix around the pressurized argon pores deforms by creep, a method, which was first described by Kearns et al. [2,3] for the alloy Ti–6Al–4V, and was further studied by others for the same alloy [4–8] and for CP-Ti [1,9–12]. For CP-Ti, we showed that this foaming technique is limited by the low creep rate of the metal which leads to sluggish pore growth [1]. To achieve a porosity level of 10%, foaming times of 20 h are needed at 980 and 950 °C, and 50 h at 903 °C; 250 h are necessary to reach a total porosity of 30% at the highest temperature studied (980 °C). Another problem is the limited ductility of CP-Ti under creeping conditions, which leads to fracture of the walls separating individual pores [1]. Pores coalescing with each other and with the specimen surface leads to escape of the pressurized gas responsible for foaming, thus limiting the maximum achievable porosity.

In previous publications [1,9–12], we showed that these two issues (low creep rate and low ductility) could be addressed by performing foaming under superplastic conditions. Rather than using microstructural superplasticity requiring fine grains, which are difficult to achieve in porous powder-metallurgy materials, we use transformation superplasticity (TSP), which occurs at all grain sizes in titanium and Ti–6Al–4V [13]. Foaming was thus performed during thermal cycling around the α/β allotropic temperature of titanium [1], where transformation superplasticity is induced by the superposition of the internal transformation stresses (due to the mismatch in density between coexisting α- and β-Ti phases) and a biasing stress, provided in this particular

* Corresponding author. Tel.: +1-847-491-5370; fax: +1-847-467-6573.
E-mail address: dunand@northwestern.edu (D.C. Dunand).
[1] Formerly N.G. Davis

1359-6454/$30.00
doi:10.1016/j.actamat.2004.01.019

case by the internal pore pressure [1]. We showed that foaming occurred much more rapidly during thermal cycling (e.g. a porosity level of 35% was achieved after 20 h) because of the higher strain rate achievable under superplastic conditions as compared to isothermal creep conditions. Also, much higher maximal porosities were achieved (as high as 44%), because of the low flow resistance and the high ductility of the pore walls, which delay pore coalescence.

The purpose of the present article is to model some of the experimental results presented in the companion paper [1], with the goal of understanding foaming under both creep and superplastic conditions. We present here two modeling methods to predict foaming behavior: an analytical model based on continuum-mechanical considerations and a numerical model using the finite element modeling (FEM).

2. Analytical modeling of pore growth

2.1. General equations

A foaming body can be thought of as an array of small pressure vessels whose internal pressure causes deformation of the vessels walls. The simplest approximation used to describe the growth of pores in a matrix is that of a single spherical pore surrounded by a spherical metallic shell with a volume fraction matching that of the metal in the foam, as illustrated in Fig. 1. The mechanics of this model was first described by Finnie and Heller [14] for the case of an infinitely thick pressure vessel and was developed for finite thickness pressure vessels by Wilkinson and Ashby [15,16] for HIPing of powder during "stage 2" consolidation, when the material is greater than 90% dense (with individual small spherical pores whose stress fields do not interact). It is assumed that the creeping solid is isotropic and that the pores are both equally spaced and spherical. Others have also used this model to describe consolidation of powders [17–20]. In addition, the creeping spherical pressure-vessel model has been used to describe cavity growth for the incubation period during hydrogen attack of steels at constant temperature and pressure, where small pores filled with methane due to reaction of hydrogen with carbon from the dissolution of carbides in the steel [21,22], and during growth of argon-filled pores by dislocation creep and grain boundary sliding in Ti–6Al–4V [8]. The following development of the relations for pore expansion is outlined in [15] for a creeping, thick-walled, pressure vessel, which was applied to powder consolidation under power-law creep conditions.

Assuming, as illustrated in Fig. 1, that the behavior of a spherical pressure vessel (representing a single pore) can describe the macroscopic behavior of the material, the relative density ρ of the vessel (and, thus, of the foam) is given by geometry as

$$\rho = \left(\frac{a}{b}\right)^3, \tag{1}$$

where a and b are the inner and outer radius of the spherical pressure vessel, respectively. The densification rate, $\dot{\rho}$, is then

$$\dot{\rho} = 3\left(\frac{a}{b}\right)^3\left(\frac{\dot{b}}{b} - \frac{\dot{a}}{a}\right). \tag{2}$$

Based on the work by Finnie and Heller [14], the following relation for the densification rate was developed by Wilkinson and Ashby [15] for the case of powder consolidation

$$\dot{\rho} = \frac{3SA}{2}\frac{\rho(1-\rho)}{\left[1-(1-\rho)^{1/n}\right]^n}\left(\frac{3}{2n}|\Delta P|\right)^n, \tag{3}$$

where $\Delta P = P_e - P_i$ is the difference between the external and internal gas pressures, $S = \mathrm{sign}(\Delta P)$ is used to alleviate any ambiguities that may arise if the power-law exponent has an even value, A is the power-law creep constant (including the activation energy term), n is the stress exponent of the wall material assumed to deform under uniaxial conditions according to a power-law

$$\dot{\varepsilon} = A\sigma^n, \tag{4}$$

where $\dot{\varepsilon}$ is the uniaxial strain rate and σ the uniaxial applied stress.

During powder consolidation, the external pressure, P_e, is greater than the internal pressure, P_i, and the

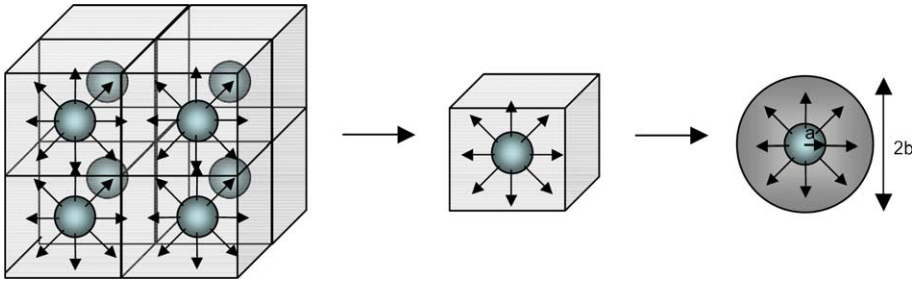

Fig. 1. Schematic showing: (left) an array of pressurized pores in a continuous matrix growing by creep deformation of the matrix; (middle) a representative volume element (RVE) containing a pore; (right) a single spherical pressure vessel with the same pore volume fraction as the RVE.

densification rate, $\dot{\rho}$, is positive. However, if P_i is greater than P_e, as in the present case of pore expansion, $\dot{\rho}$ is negative. Using the pore volume fraction f (also called porosity in the following) as

$$f = 1 - \rho \tag{5a}$$

the foaming rate, $\dot{f}$, is then

$$\dot{f} = -\dot{\rho}. \tag{5b}$$

Introducing Eqs. (5a) and (5b) into Eq. (3) and rearranging leads to

$$\dot{f} = \frac{3A}{2}\frac{f(1-f)}{\left[1-f^{1/n}\right]^n}\left(\frac{3}{2n}|\Delta P|\right)^n. \tag{6}$$

For the gas pressure difference, $\Delta P = P_e - P_i$, the external pressure, P_e, is constant (in our case it is atmospheric pressure, $P_e = 0.1013$ MPa), but the internal pressure, P_i, is continuously evolving during changes in temperature and during pore growth. Using the ideal gas law, the internal pore pressure, P_i, can be written in term of the initial pore pressure, P_0, the initial temperature, T_0, the initial pore fraction, f_0, and the foaming temperature, T, as

$$P_i = P_0\frac{f_0}{1-f_0}\frac{1-f}{f}\frac{T}{T_0}. \tag{7}$$

The initial pore pressure and temperature are taken from the HIP conditions ($P_0 = 100$ MPa and $T_0 = 890$ °C), and the initial pore fraction is

$$f_0 = 1 - \left(\frac{a_0}{b_0}\right)^3, \tag{8}$$

where a_0 and b_0 are the initial inner and outer radius of the spherical pressure vessel, respectively. In the present study, an initial pore fraction $f_0 = 0.14\%$ was used, as measured by the Archimedes method on the as-HIPed samples [1].

2.2. Isothermal foaming

For the first case to be modeled, where argon pores expand in titanium at a constant temperature, deformation by climb-controlled power-law creep is assumed, so $n = 4.3$ [23] can be used in Eq. (6). The power-law creep exponent A_{pl} depends on temperature as [23]

$$A_{pl} = \frac{A_2 D_{eff} b}{kT\mu^{n-1}}, \tag{9}$$

where A_2 is the Dorn constant, b is the Burgers vector, μ is the shear modulus, and D_{eff} is the effective diffusion coefficient. At high temperatures, lattice diffusion dominates creep deformation and the effective diffusion coefficient can be approximated to equal the volume diffusion coeffiecient, D_v, which varies with temperature as [23]

$$D_v = D_{ov}\exp\left(\frac{-Q_v}{RT}\right), \tag{10}$$

where Q_v is the activation energy for volume diffusion and D_{ov} is the lattice diffusion pre-exponential constant. The shear modulus is also temperature-dependent [23]

$$\mu(T) = \mu_0\left(1 + \left(\frac{T-300}{T_m}\right)\left(\frac{T_m}{\mu_0}\frac{d\mu}{dT}\right)\right), \tag{11}$$

where T_m is the melting temperature. The constants, A_2, b, D_{ov}, Q_v, μ_0, and $(T_m/\mu_0)(d\mu/dT)$, take different values for α- and β-Ti [23].

During the early stages of foaming when the pressure inside the pore is large (100 MPa), pore growth likely occurs by glide-controlled creep (power-law break down) before making a transition to climb-controlled creep at lower stress (pore pressure) where power-law creep as described by Eq. (4) is used. While both regions can be described using a hyperbolic sine creep law, in most cases (except at higher Ar backfill pressures) by the time the specimens have reached 1% porosity, the pore pressure is sufficiently small for the deformation to be described simply by power-law creep. The contribution to pore growth by glide-controlled creep will be ignored and only described using the power-law relation, which produces a small underestimate of the deformation rate. Similarly, deformation by diffusional creep is not considered due to the large grain sizes (well above the 10 μm critical grain size for grain boundary sliding [24]) observed in the titanium foams.

Introducing Eqs. (7)–(11) into Eq. (6), the foaming rate equation for isothermal foaming under power-law condition becomes

$$\dot{f}(t)_{iso} = \left(\frac{3}{2}\right)^{5.3}\frac{A_2 D_{ov}\exp\left(\frac{-Q_v}{RT}\right)b}{kT\mu_0^{3.3}\left(1+\left(\frac{T-300}{T_m}\right)\left(\frac{T_m}{\mu_0}\frac{d\mu}{dT}\right)\right)^{3.3}} \times \frac{f(1-f)}{\left[1-f^{1/4.3}\right]^{4.3}}\left(\frac{1}{4.3}\left|P_e - P_0\frac{f_0}{1-f_0}\frac{1-f}{f}\frac{T}{T_0}\right|\right)^{4.3}. \tag{12}$$

Eq. (12) is a differential equation for the porosity f, which includes processing parameters (initial temperature and initial pore fraction and pore pressure), foaming parameters (foaming temperature and external pressure) and material physical and creep parameters, all of which are experimentally accessible.

2.3. Thermal cycling foaming

For the second case where titanium is foamed by thermal cycling through the α/β-phase transformation, transformation superplasticity is another active deformation mechanism with the following uniaxial deformation law:

$$\dot{\varepsilon} = A_{TSP}\sigma, \tag{13}$$

where A_{TSP} is

$$A_{TSP} = \frac{4}{3}\frac{\Delta V}{V}\frac{1}{\sigma_0}\frac{5n}{4n+1}\frac{1}{\Delta t}, \tag{14}$$

where $\Delta V/V$ is the volume mismatch between the two phases of titanium, σ_0 is the average internal stress during transformation and Δt is the time interval for the transformation [25]. A value of $A_{TSP} = 2.3(\mathrm{GPa}^{-1})/\Delta t$ for CP-Ti was found under uniaxial tension in three different studies (as summarized in [26]) and has been used previously to accurately model TSP deformation such as multiaxial doaming of CP-Ti, Ti–6Al–4V and their composites by thermal cycling [27] as well as densification of metal powders by thermal cycling [20]. A_{TSP} is independent of temperature, as TSP is only operative during the phase transformation.

Introducing Eq. (13) into Eq. (6) with $n = 1$ and $A = A_{TSP}$, the foaming rate for thermal cycling under TSP condition becomes

$$\dot{f}(t)_{TSP} = \frac{9A_{TSP}}{4} f\left(\left|P_e - P_0\frac{f_0}{1-f_0}\frac{1-f}{f}\frac{T}{T_0}\right|\right). \tag{15}$$

Since thermal cycles typically extend above and below the transformation temperature, two deformation mechanisms can be considered to take place independently and sequentially during the thermal cycle: transformation superplasticity within, and creep outside the transformation range. Then, the total foaming rate can be approximated as the sum of the foaming rate due to creep outside the transformation range (Eq. (12)) and that due to TSP in the transformation range (Eq. (15))

$$\dot{f}_{cyc} = \dot{f}(t)_{iso} + \dot{f}(t)_{TSP}. \tag{16}$$

Eq. (16) can then be integrated to find $f(t)$, while setting to zero either contribution in the right-hand side of the equation, when those mechanisms are not active.

2.4. Computational procedures

No closed-form solution exists for Eqs. (12) and (16) which were solved numerically to find the porosity as a function of time, $f(t)$. Using materials parameter from [23], the equations were iteratively solved using an adaptive, step-size, non-stiff Adams method or a stiff Gear method based on Least Square Ordinary Differential Equation.

First, the porosity accumulated during the initial temperature excursion from room temperature to foaming temperature was calculated, using heating rates $T(t) = 75$ or 15 °C/min in Eqs. (12) and (16), depending on the experimental data used for comparison. This porosity was then added to that accumulated during subsequent foaming. For isothermal foaming, this was achieved by solving Eq. (12) at the isothermal foaming temperature. For thermal cycling foaming, Eq. (16) was solved using the effective temperature of the thermal cycle for Eq. (4). The effective temperature, T_{eff}, is defined as the temperature at which the isothermal creep rate is the same as the time-averaged creep rate during thermal cycling in the absence of TSP [28,29], and was calculated using creep activation energies given in [23] for α-Ti and β-Ti. This approach, which spreads the TSP contribution over the whole cycle, allows the use of a single temperature $T = T_{eff}$ to solve Eq. (16), thus considerably simplifying the calculations, as compared to using the true cycling profile, for which each cycle would need to be considered.

The choice of temperature does not affect the uniaxial TSP strain contribution as A_{TSP} is temperature-independent, but it has an effect on the pore pressure (Eq. (7)); the error in using T_{eff} rather than the true transformation temperature in Eq. (16) is expected to be negligible. Similarly, the pressure variation associated with the temperature cycle is averaged during the creep calculations. The isothermal creep contribution in using Eq. (16) with $T = T_{eff}$ is slightly over-estimated, as during the cycle there is no creep during the phase transformation. However, the error is insignificant as the transformation is expected to take place rapidly.

3. Numerical modeling of pore growth

3.1. Representative volume element

We model the foam as a regularly stacked hexagonal array of prisms, each containing a pore in their center. The prism is approximated by a cylinder, as shown schematically in Fig. 2. The cylinder is a common representative volume element (RVE) used in FEM to approximate void growth during uniaxial tension of ductile metals [30–35] and polymers [36,37] and for flow of metal- [38–40] or polymer- [41] matrix composites with whisker or particulate reinforcement. The axisymmetric cylinder is used rather than a space-filling array of prisms, due to the computationally intensive nature of three-dimensional space-filled modeling as compared with using the cylindrical axisymmetric approximation, which is generally considered to lead to only minor errors [30,32–35,39]. In the previous cited cases, where the axisymmetric models were used to model either void growth or material behavior in the presence of voids, particulates or whiskers, a constant, remote state of stress was applied to the cylinder. For the present case of pore growth due to internal pressure, different loading conditions were applied.

The RVEs used for modeling the case of spherical pores growing due to internal pore pressure by TSP and/or creep of a titanium matrix surrounding the pores are shown in Figs. 3(a) and (b). Fig. 3(a) is the basis for most of the following analyses where a single pore size is modeled. The pores have an initial radius, r_0, and the

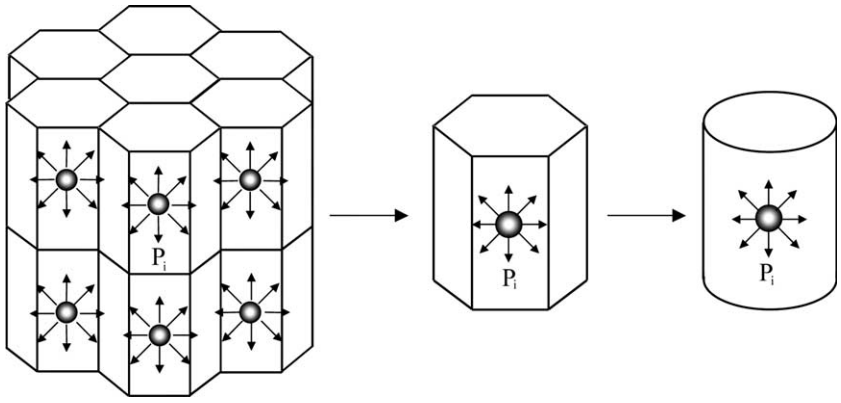

Fig. 2. Schematic showing how the axisymmetric RVE with repeating boundary conditions approximates a space-filling three-dimensional array of pores within prisms.

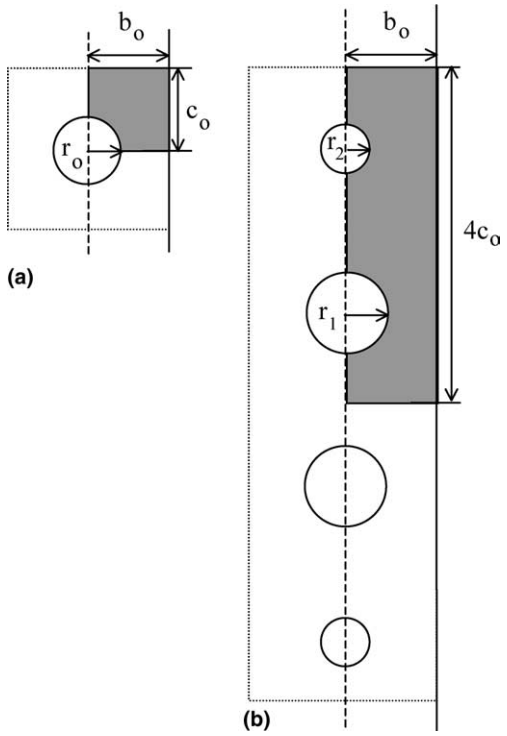

Fig. 3. Schematic of axisymmetric model used for modeling pore growth of (a) one pore, where only the upper half of a pore is modeled; (b) for two pores of different sizes where both pore are entirely modeled. Pore volume fraction is ca. 5%.

center of the pore is taken to be at the center of the cylindrical RVE. Running length-wise down the center of the RVE is the axis of symmetry, and perpendicular to it is a mirror plane, which cuts the cylinder and pore in half. Due to symmetry, only the shaded portion of the cylinder in Fig. 3(a) needs to be modeled. The cylinder is characterized by a radius b_0 and a height c_0.

For the case of modeling the pore growth of a single pore size that is comparable to the data displayed in the current publication, an initial value $r_0 = 7.5$ μm is given and b_0 and c_0 are chosen to maintain the given initial porosity, $f_0 = 0.14\%$. The initial spacing between the pores is $2b_0$ in the radial direction and $2c_0$ axially. Homogeneous boundary conditions are applied to the surface of the cylinder requiring that during pore growth the displacements are constrained such that the RVE remains cylindrical, so as not to overlap during pore growth with the "adjacent" RVE, which is not explicitly modeled, but considered to be taken into account by the homogeneous boundary conditions. In such a way, a good approximation of a regularly stacked hexagonal array of prisms is achieved, taking into account stress field interaction between adjacent pores. This is one of the main improvements as compared to the analytical pressure-vessel model presented above, where the outer surface of the spherical vessel is assumed traction-free.

Three RVEs based on the one shown in Fig. 3(a) were used to study the effect of irregular pore spacing on the foaming rate. Three different cylindrical aspect ratios were studied: $c_0/b_0 = 1$, 3 and 5. Each aspect ratio was modeled under isothermal (power-law creep only) and thermal cycling (power-law creep and TSP) conditions and, in all cases, the initial porosity was taken as $f_0 = 0.14\%$ and the initial pore size as $r_0 = 7.5$ μm. An example of a meshed RVE with $c_0/b_0 = 1$ is shown in Fig. 4.

The effect of various pore sizes within a porous preform upon the foaming rate was explored by using the RVE in Fig. 3(b) where each pore is equidistant (center-to-center) from all other neighboring pores in all directions. In this case, one pore was larger ($r_1 \sim 9$ μm) and the other pore was smaller ($r_2 \sim 4.5$ μm) than that used in the modeling of equi-sized pores ($r_0 = 7.5$ μm), such that the ratio of the volume of the larger pore to the smaller pore was initially 8. The initial porosity of the RVE remained the same as for equi-sized pore modeling (i.e., $2r_0^3 = r_1^3 + r_2^3$). In this case, a larger RVE was used (Fig. 3(b)) where both pores are considered fully. The

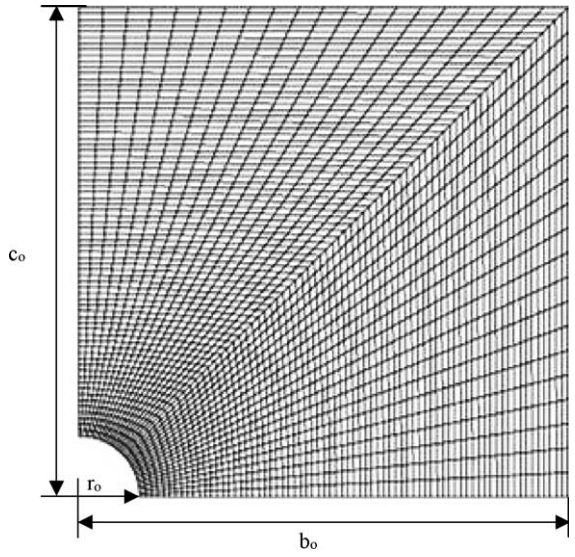

Fig. 4. Example of a meshed RVE with an initial porosity $f_0 = 0.14\%$ and $c_0/b_0 = 1$ for the axisymmetric RVE used in the study of pore growth.

radius of the RVE remains b_0 but the height is now $4c_0$ such that the spacing between the pore centers remains the same as for the case in Fig. 3(a) where c_0/b_0 was unity. The case of isothermal foaming and thermal cycling were studied. Again, the dashed line in Fig. 3(b) is constrained as an axis of symmetry and homogeneous boundary conditions were applied to the same surfaces as for the RVE in Fig. 3(a), such that the RVE remained cylindrical, with the bottom plane as a mirror plane.

All of these simple RVEs discussed above are approximations and idealizations of the more complex foam structure. In a real porous structure, the shape of the pores are irregular, even after HIPing and of varying sizes and distance to neighboring pores [1]. During foaming under both isothermal and thermal cycling conditions, pores merge, further changing the pore shape and, therefore, the stress distribution surrounding the pores. Additionally, pores are not aligned on regular arrays, but rather are distributed randomly in space, as the powders were randomly arranged prior to HIPing.

3.2. Computational procedures

A commercial FEM package [42] was used for all modeling. The titanium matrix was discretized using axisymmetric continuum elements (with reduced integration and hourglass control for integrity during large displacements) and the pore was modeled using hydrostatic fluid elements applied to its surface. The hydrostatic fluid elements allowed for the pressure inside the pore to be adjusted with pore growth. The amount of "fluid" inside the pore was constrained to be constant during the analysis, requiring that the pore pressure decrease as the pores grow. Both the pore and the RVE were allowed to expand so that a total volume increase of the RVE was observed during pore growth.

The thermal cycle initially modeled with FEM was chosen to be a triangular cycle with upper and lower temperatures of 830 and 980 °C and a 4 min period, for which the maximum porosity of 44% was observed experimentally [1]. Modeling of the titanium material properties during foaming for the case of thermal cycling was performed by adding the uniaxial strain-rates under TSP and under power-law creep conditions at 903 °C, the effective temperature of the thermal cycle, such that

$$\dot{\varepsilon}_{\text{tot}} = A_{\text{pl}}\sigma^n + A_{\text{TSP}}\sigma \tag{17}$$

using a user-defined sub-routine, where A_{pl} and A_{TSP} have the same meaning as for the pressure-vessel model. This is the same approach taken for the pressure-vessel model (Eq. (12)) and the same limitations discussed earlier apply here.

Material properties for titanium under uniaxial conditions for creep [23] and TSP [26] were used. As mentioned earlier, uniaxial creep and TSP constants have been used previously to successfully model multiaxial deformation in titanium, titanium alloys and their composites [43] under both creep and TSP conditions. For each analysis, it was assumed that the gas within each pore reached equilibrium with the HIP pressure (100 MPa) during HIPing at 890 °C and the initial pore pressure used for modeling was taken to be the pressure at 903 °C (101 MPa) so that, unlike the pressure-vessel modeling, it is assumed that there is no expansion during heating to 903 °C (i.e., heating is instantaneous). During each analysis, pore volume and pressure, as well as the displacements of various nodes were recorded to monitor the pore and RVE aspect ratios.

Due to the current limitations of the software, most foaming curves $f(t)$ had to be computed in two parts. At the high initial pore pressures, high strain rates produced large nodal displacements. The model could not be re-meshed and restarted automatically, because of the necessity to use hydrostatic fluid elements, to achieve automatic adjustment of pore pressure with its growth; hydrostatic fluid elements are incapable of being re-meshed automatically. Rather, after reaching about 2% porosity, the deformed RVE was redrawn and re-meshed, and a new calculation initiated, using as initial pore pressure the value achieved at the end of the first computation. This procedure was not repeated. RVEs with two pores did not require re-meshing. Using a Pentium II, 400 MHz Window NT computer, analysis for the typical single pore RVE (Fig. 3(a)) had a wall clock time of about 8 h to model 60 h of foaming, while those for the two-pore RVE (Fig. 3(b)) required about 24 h computation to model 5 h of foaming.

4. Results and discussion

4.1. Pressure-vessel model predictions

Foaming curves, where porosity f is plotted as a function of time, are plotted in Figs. 5(a)–(d) as calculated from Eqs. (12) and (16). Due to the scale of the graphs, the heating portion of the curve (which is near horizontal) is not visible behind the data point near the origin.

For the case of isothermal foaming, predictions from Eq. (12) match the experimental porosity data [1] for 903 °C (Figs. 5(a) and (c)) and 955 °C (Fig. 5(d)), up to the relatively modest porosity level of 10%. For porosity greater than 10%, and up to the maximal experimental porosity of 17% in Fig. 5(d), the model somewhat underestimates the observed porosity. The error is, however, acceptable, given uncertainties in materials creep constants and initial parameters.

For thermal cycling superplastic conditions, the foaming curves calculated with Eq. (16) overlap with the calculated isothermal creep curves (Eq. (12)) at low porosity values in Figs. 5(a), (c), and (d), as expected from the fact that creep is much more rapid than TSP at high stresses, when the pore pressure is high. The effect of superplasticity becomes apparent as a departure of the TSP foaming curves from the creep foaming curves in Figs. 5(a), (c), and (d), which occurs at earlier times (and lower porosity), the faster the cycling rate and thus the larger the TSP contribution, as expected. Figs. 5(a) and (c) are qualitatively consistent with data trend for the 830–980 °C/4 min, and 830–980 °C/20 min thermal cycles. The TSP model predicts similarly well how changing the effective temperature of the thermal cycle (by increasing the maximum temperature of the thermal cycle at constant heating/cooling rate) affects the trends in the foaming curves, as shown in Figs. 5(b)–(d) where the TSP model predictions are compared to experimental data for thermal cycles of 830–930 °C/13 min, 830–980 °C/20 min, and 830–1050 °C/30 min, respectively. While the TSP predictions are able to capture the general shape of the experimental foaming curves during thermal cycling, the magnitude of the porosity is underpredicted by a factor of about two.

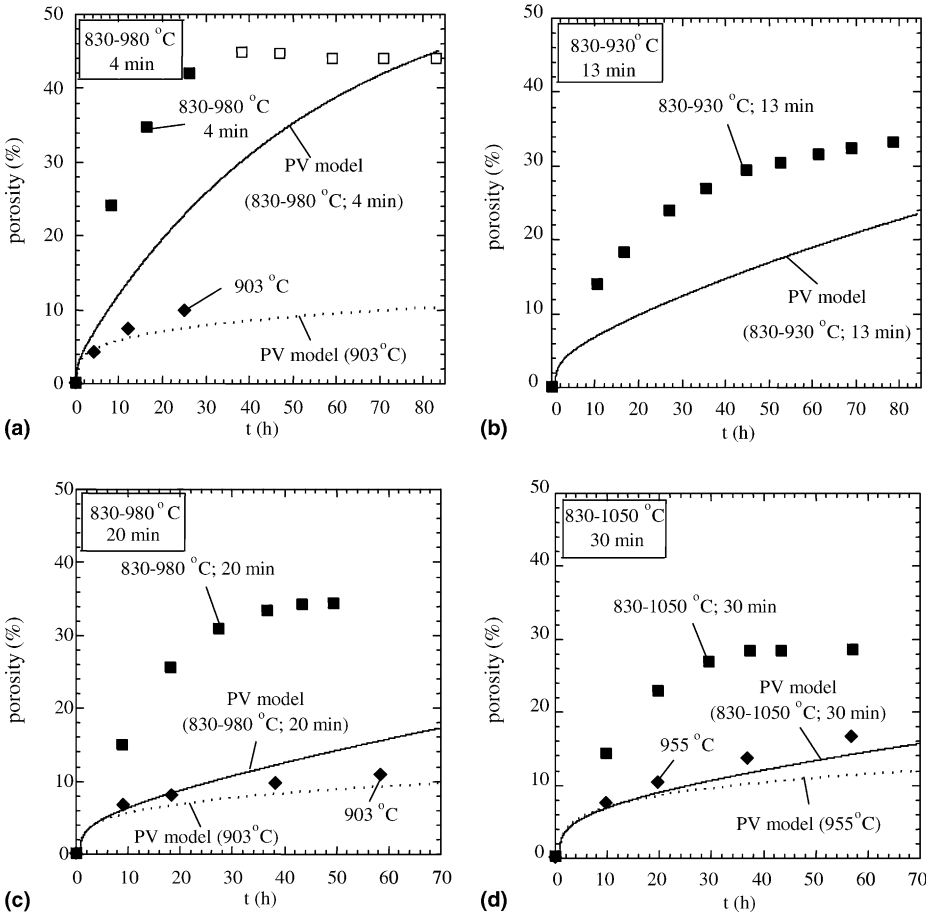

Fig. 5. Pressure-vessel model predictions for the foaming curves under various thermal cycling conditions (solid lines) and isothermal anneals at the cycle effective temperature (dotted lines) compared to experimental data [1] (points): (a) 4 min cycles, 830–980 °C (903 °C), (b) 13 min cycles, 830–930 °C, (c) 20 min cycles, 830–980 °C (903 °C), (d) 30 min cycles, 830–1050 °C (955 °C).

One possible source of error is the value for initial porosity ($f_0 = 0.14\%$), which was measured experimentally by Archimedes density measurements [1]. However, this value may have errors as large as $\pm 0.11\%$ porosity (i.e., f_0 could be as low as 0.03% or as high as 0.25%), due to the uncertainty in the density of CP-Ti to more than three significant digits ($\rho_{Ti} = 4.51$ g/cm^3 is used, but the value could be 4.505 or 4.515 g/cm^3). To investigate the effect of initial porosity, curves were calculated for various values of initial porosity above and below the nominal value $f_0 = 0.14\%$ for the thermal conditions of Fig. 5(a). Assuming a value $f_0 = 0.20\%$ (well within the experimental error) shifts the foaming curves towards higher values, decreasing by ca. half the discrepancy with respect to the TSP data shown in Fig. 5(a) [44]. Another set of calculations for various initial pressures showed that the maximal estimated experimental error of 5 MPa had only a very small effect on the calculated curves of Fig. 5(a) [44].

There must be other sources for the underestimation of the TSP model in Figs. 5(a)–(d) beyond the errors in initial porosity and pressure. Other possible reasons include: (i) overlapping of stress fields from neighboring pores, resulting in higher stress in the pore wall material than calculated with the present model assuming no pore interactions; (ii) non-uniform spatial distribution of pores leading to stress concentrations in areas where pores are clustered; (iii) distribution of pore sizes, also leading to local stress concentrations and more rapid pore growth; (iv) non-spherical pore shape, which may produce more rapid pore growth, especially in conjunction with the other effects listed above producing stress concentrations; (v) pore merging leading to highly non-spherical growing more quickly than the parent pores before merging; (vi) additional internal stresses (assisting the transformation stresses in producing TSP) as a result of thermal gradients because of the poor thermal conductivity of foamed titanium; (vii) more rapid creep deformation mechanisms during the creep portion of the cycle, e.g., power-law breakdown at high stresses, diffusional creep at low stresses, and cavitation at high strains. We note that the above effects will induce relatively small errors at the low porosity values observed during isothermal foaming, which may explain why predictions of Eq. (12) are in better agreement with data than those of Eq. (16), where experimental porosity reaches values as high as 44%.

Furthermore, because the model makes no allowance for pore opening to the specimen surface, it cannot predict the decrease (and eventual cessation) in foaming due to gas loss by pore surface opening, which is observed experimentally as open porosity [1] and which leads to the plateau in Figs. 5(a)–(d). The purpose of the numerical calculations described in the following section is to explore the effects (i)–(iii) listed above.

4.2. FEM predictions

4.2.1. Single equi-sized pore

Foaming curves as calculated by FEM for the case of a single, equi-sized pore ($c_0/b_0 = 1$) are compared with experimental data and pressure-vessel model predictions in Fig. 6 for both isothermal and thermal cycling conditions. In this figure, porosity accrued during the heating ramp was not included for the pressure-vessel predictions, to allow a direct comparison with FEM results which also exclude the heating ramp; this error is insignificant, as can be seen from the very small porosity increase accumulated during ramp times plotted in Figs. 5(a)–(d). For the case of isothermal creep, there is excellent agreement between the FEM predictions and the predictions from the pressure-vessel model. Also, under thermal cycling conditions, FEM results match the predictions from the pressure-vessel model well, with the FEM curve shifted to slightly higher porosity values. Thus, the overlapping of stress fields from neighboring pores, which is taken into account in the FEM predictions but not in the pressure-vessel calculations, has little overall effect on the foaming curves of Fig. 6, and cannot explain the discrepancy between predictions and thermal cycling data.

Fig. 7 shows the von Mises matrix stress in the RVE, in the form of stress contour maps, for foaming under thermal cycling conditions (830–980 °C/4 min), where deformation is induced both by TSP (during transformation) and power-law creep (in the β-Ti field). The effect of stress field overlap between adjacent pores is visible as deviation from a circular shape for the stress contour, illustrating that this effect becomes the more important the farther from the pore surface, as expected. The slight radial asymmetry of the stress contours shown in Fig. 7 is due to the choice of the cylindrical

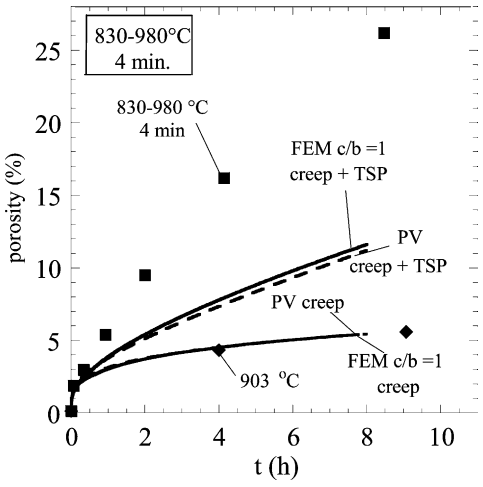

Fig. 6. FEM predictions for foaming curves under thermal cycling (830–980 °C/4 min) and isothermal conditions (903 °C), compared to experimental data [1] and pressure-vessel (PV) model predictions.

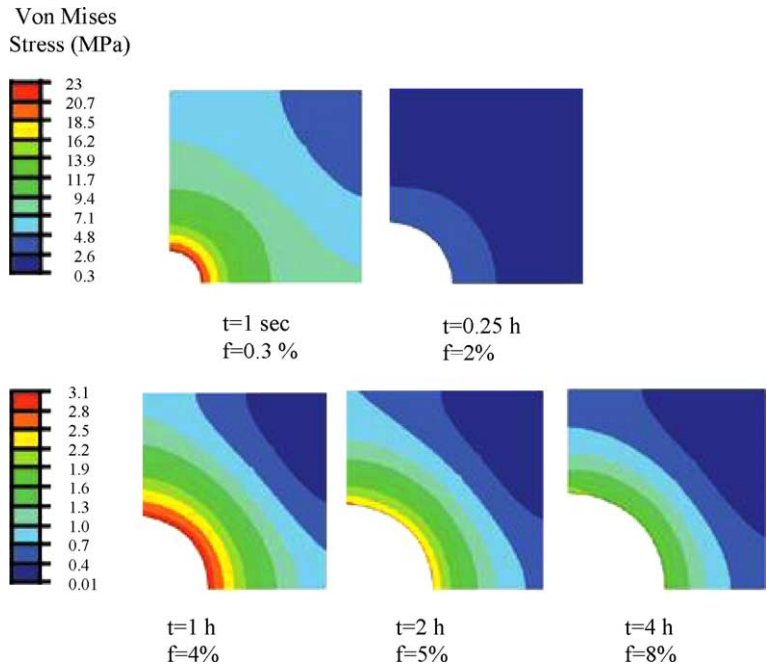

Fig. 7. FEM predictions for the von Mises stress distribution during foaming under thermal cycling conditions (830–980 °C/4 min) for a preform with an initial porosity $f_0 = 0.14\%$ and $c_0/b_0 = 1$ after 1 s, 0.25, 1, 2 and 4 h of thermal cycling.

RVE, which does not share the spherically symmetry of the pore.

After 1 s of foaming, Fig. 7 shows that the porosity is over twice the original value $f_0 = 0.14\%$ and the maximum von Mises stress value at the pore surface has dropped significantly from ca. 100 to 23 MPa due to the drop in pore pressure from the original value of ca. 100 MPa. After 15 min of foaming, the pore volume has further grown by a factor ca. 7 (the pore pressure has dropped by the same factor) and the stress in most of the matrix volume is below 2.6 MPa. After 1 h of foaming (corresponding to fifteen 4-min cycles between 830 and 980 °C) the porosity has further doubled, and the matrix stress has dropped below 2 MPa in most of the matrix volume. This stress range, below ca. 2.5 MPa, is where TSP emerges as a deformation mechanism more rapid than creep in uniaxial tension test of CP-Ti [26,29], which is reflected in Fig. 6 by a departure of the TSP foaming curve from the isothermal foaming curve. After a final quadrupling in time to 4 h, the porosity has doubled to 8%, and is almost twice that under creep conditions; the von Mises stress in the whole volume is below ca. 2.2 MPa, so that TSP dominates over creep everywhere in the RVE.

As mentioned earlier, the predicted foaming curves for the pressure-vessel and FEM model are quite close (Fig. 6), so that the much larger time investment for the FEM model may seem unnecessary. This somewhat unexpected result could not have been predicted a priori and may only be valid for the present experimental parameters. Also, the complex stress distribution in Fig. 7 predicted by the FEM model illustrates that FEM is a valuable tool for a better understanding of the deformation mechanisms occurring during foaming. Finally, as described in the following sections, FEM allows for the exploration of pore spatial distribution and size distribution.

4.2.2. Pore clustering

Figs. 8(a) and (b) show FEM foaming curves using RVEs with varying c_0/b_0 aspect ratios (and constant $r_0 = 7.5$ μm) for both thermal cycling and isothermal foaming. Increasing the aspect ratio of the RVE, which translates into decreasing the pore spacing along the radial direction and increasing their spacing along the axial directions, result in a noticeable increase in pore growth rate for both isothermal foaming and thermal cycling.

For isothermal foaming (Fig. 8(b)), all modified RVEs over-predict the experimental porosity. However, for the case of thermal cycling (Fig. 8(a)), the modified RVE with $c_0/b_0 = 5$ matches the experimental data much better than for the case of equidistant pores with $c_0/b_0 = 1$. Since the pore distribution was the same for both experiments, pore clustering ($c_0/b_0 = 5$) cannot be invoked to match prediction to the TSP data, while not invoking it ($c_0/b_0 = 1$) for the isothermal case.

An improvement between data and model for Fig. 8(a) can be achieved if a modified value of A_{TSP} is used to describe the TSP behavior (Eq. (14)) with an RVE aspect ratio of unity, as shown in Fig. 8(a). In this case, a good match between data and prediction is

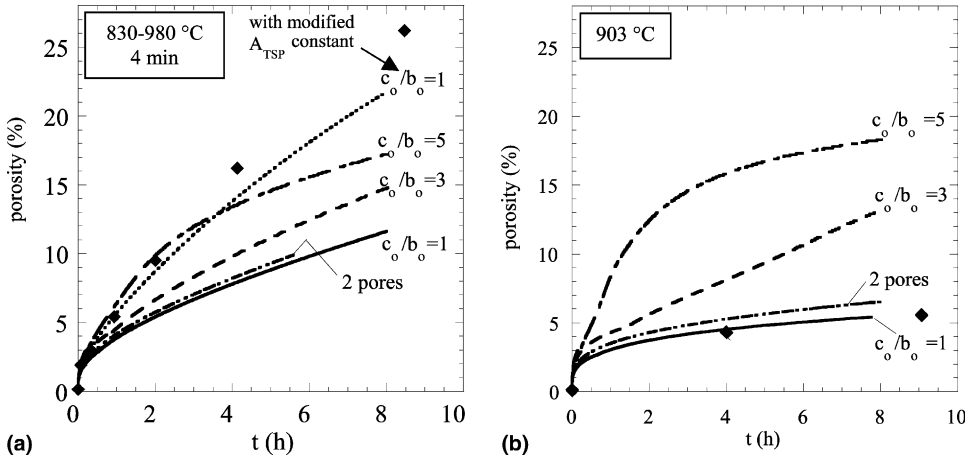

Fig. 8. FEM predictions (lines) for the foaming curves using RVE with various aspect ratio and number of pores compared to experimental data [1] (points) for (a) 830–980 °C/4 min thermal cycling and (b) isothermal foaming at 903 °C.

achieved if the value of A_{TSP} is multiplied by a factor 3. It should be noted, however, that the value of the A_{TSP} for CP-Ti is characterized within a factor of ca. 1.5 [25,26,29] under uniaxial conditions, so that this correction cannot fully explain the discrepancy. Also, the uniaxial value of A_{TSP} has been used previously to describe and model multiaxial deformation due to TSP under similar thermal cycling conditions [43], so it is unlikely that the error originates from the multiaxial state of stress. However, it is conceivable that a combination of increased A_{TSP} within the allowed range of 1.5 and mild pore clustering could explain most of the discrepancy between model and data in Fig. 8(a), while maintaining the good fit in Fig. 8(b).

The enhancement in foaming rate due to the irregular pore spacing ($c_0/b_0 > 1$) can be further investigated by comparing the von Mises stress-states in each case after 5 h of isothermal foaming under isothermal or thermal cycling conditions, as shown in Fig. 9. The reduced radial spacing between the pores for $c_0/b_0 > 1$ creates strong stress concentrations in the thin pore walls, as a result of stress field overlap between adjacent pores. Conversely, the stress fields in the longitudinal direction do not overlap significantly. As a result, the pore grows more in height (c-direction) by extensive deformation of the thin, highly stressed pore wall and the pore becomes elongated as pore growth continues.

The aspect ratio of the pores r_c/r_b (where r_c and r_b are the pore radii along the c- and b-directions) and the RVE aspect ratio c/b (normalized by the original aspect ratio c_0/b_0) after 5 h of foaming is summarized in Table 1. This table shows that, for RVEs with a single, unclustered pore ($c_0/b_0 = 1$), both the pore and the RVE remain equiaxed under either creeping or superplastic conditions. However, when the pores are clustered (for $c_0/b_0 > 1$), both the pore and the RVE grow in an anisotropic manner. This theoretical result indicates that

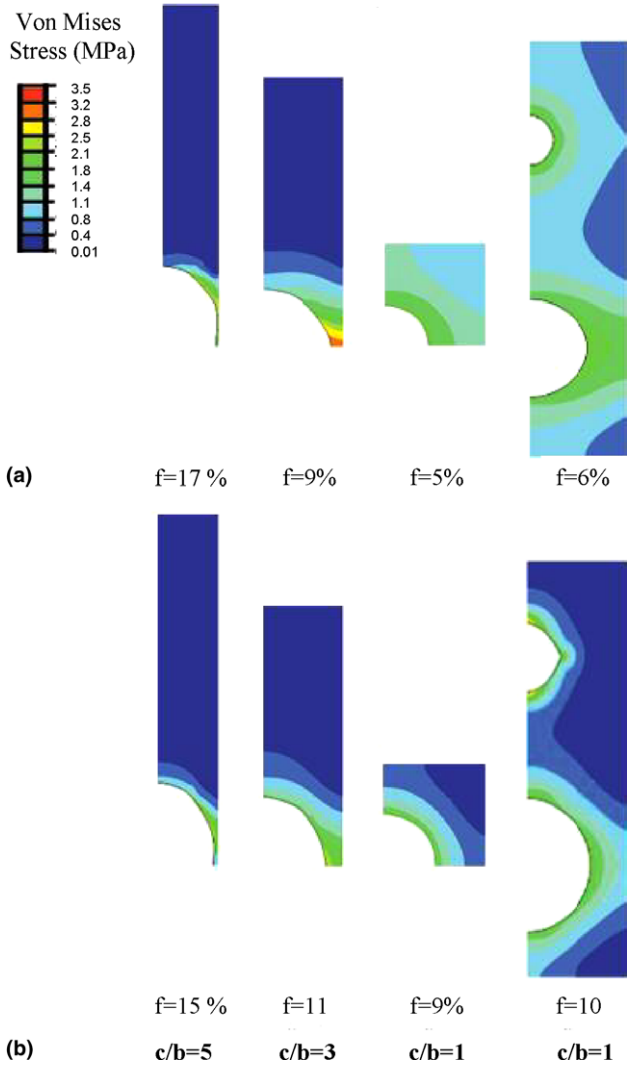

Fig. 9. FEM predictions for the von Mises stress distribution after 5 h of foaming. (a) Isothermal foaming (creep, 903 °C); (b) thermal cycling foaming (superplasticity and creep, 830–980 °C/4 min). All RVEs had an initial porosity of 0.14%.

Table 1
Aspect ratios for pores (r_c/r_b) and for RVE (c/b, normalized by c_0/b_0) as predicted by FEM after 5 h of foaming under isothermal or cycling conditions

		$c_0/b_0 = 1$	$c_0/b_0 = 3$	$c_0/b_0 = 5$	$c_0/b_0 = 1$ Small pore	$c_0/b_0 = 1$ Large pore
r_c/r_b	Isothermal	1.02	1.10	1.50	1.03	0.84
	Cycling	1.00	1.10	1.43	1.02	1.02
$(c/b)/(c_0/b_0)$	Isothermal	1.02	1.12	1.20	1.04	
	Cycling	1.00	1.09	1.20	1.04	

initially spherical pores can become quite elongated if they are clustered or aligned (either by design or by chance during powder processing). The resulting anisotropy in pore wall thickness and shape could create a material with mechanical properties that are directionally dependent. There is no significant difference in the predicted aspect ratios after 5 h of foaming between isothermal and thermal cycling conditions, which is expected due to the similarity between the foaming rates for thermal cycling and isothermal foaming for RVE's with $c_0/b_0 > 1$ (Figs. 8(a) and (b)).

For $c_0/b_0 = 1$ or 3, the pores grow faster under thermal cycling superplastic conditions as compared to growth under isothermal creeping conditions, as can be seen from the foaming curves in Figs. 8(a) and (b). This results in a lower pore pressure after 5 h of thermal cycling and, therefore, a lower state of stress in the matrix, as seen in Fig. 9. The enhancement in foaming rate due to TSP decreases with c_0/b_0 increasing from 1 to 3 (Fig. 8). This is similar to experimental data [44] showing that, for preforms with initially thin pore walls, the enhancement due to thermal cycling is minimal. However, for $c_0/b_0 = 5$, the foaming curve for isothermal conditions is somewhat faster than for thermal cycling conditions (Fig. 8). This is unphysical as, even in the extreme case where TSP would yield no enhancement to deformation, the two foaming curves should overlap. Therefore, this discrepancy must be due to errors, which most probably occurred during the manual re-meshing procedure.

4.2.3. Pore size distribution

Also shown in Figs. 8(a) and (b) are foaming curves calculated for the case where the matrix contains pores of two different sizes, with a RVE shown in Fig. 3(b) exhibiting the same initial average porosity and pore center-to-center distance as the single pore RVE with $c_0/b_0 = 1$ (Fig. 3(a)). The two-pore RVE shows a foaming rate only marginally faster than the single pore RVE, indicating that pore size distribution has only a minor effect on the foaming rate. As compared to the single pore case, the stress concentration is enhanced between the larger pores and reduced between the smaller pores in both horizontal and vertical directions, as illustrated in Fig. 9. All pores are near equiaxed after 5 h of foaming, as for the single pore case, except for the larger pore under creep conditions, which has an aspect ratio of 0.84 (Table 1). This result was unexpected and may be due to the complex interactions between the overlapping stress fields of both small and large pores. Finally, the small stress concentration present at the equator of the small pore deforming by TSP in Fig. 9 is most probably a numerical artifact.

4.2.4. Limitations of model

The FEM approach is a more realistic method for the modeling of solid-state foaming than the analytical approach, by removing limitations (i)–(iii) listed in the previous section. However, limitations (iv)–(vi) remain, and may explain why the current FEM results do not absolutely reproduce experimental data, in particular under thermal cycling conditions. Some of the model limitations are inherent in continuum-mechanical modeling, such as assuming a periodic array of pores in space. Pore coalescence and opening to the surface (open porosity) are not able to be modeled using current methods.

More sophisticated boundary conditions could be applied, e.g., a staggered stacking of with BCC symmetry [41], truncated axisymmetric cylinders [37], or Voronoi tessellation, where the pore spacing is different in the radial and axial directions. Furthermore, the axisymmetric model used here due to limited computing power is expected to generate increasingly important error as compared to a true space-filling cubic RVE.

Also, for modeling of thermal cycling, the effects of isothermal creep at 903 °C (the effective temperature for the thermal cycling) and of TSP were added, as the two mechanisms are independent and occur at different times during the thermal cycle. Thus, the thermal cycles were not explicitly modeled. Since the enhancement due to TSP is most significant in the presence of small stresses, even a factor as minor as the stresses due to the presence of thermal gradients present during thermal cycling, could cause significant superplastic effects. Additionally, the presence of thermal gradients could change the phase transformation kinetics and create a phase front within the specimen, which could lead to a change in the pore growth properties as compared to a transformation by homogenous nucleation and growth in the sample volume. Due to the lowered thermal conductivity of metallic foam as compared to bulk metals, thermal

gradients effect may become important at high levels of porosity.

5. Conclusions

Models for the time dependence of porosity during solid-state foaming of a metal containing pressurized pores have been developed under thermal cycling, superplastic conditions or under isothermal, creep conditions.

1. An existing continuum-mechanical analytical model based on creep of a spherical pressure vessel has been modified for the case where creep and transformation superplasticity occur sequentially during thermal cycling. Additionally, pore growth during initial heating from ambient temperature was modeled by considering the temperature dependence of the internal pore pressure and material properties. Good quantitative agreement between model predictions and experimental data was found for the case of isothermal foaming, and qualitative experimental trends with varying thermal cycling time and temperatures were predicted for foaming under thermal cycling conditions.

2. The finite element method (FEM) was applied to a representative volume element (RVE) consisting of an axisymmetric cylinder containing a spherical, pressurized pore in its center with homogeneous boundary conditions applied to its surface. FEM predictions for pore growth were in good agreement with the analytical pressure-vessel model and experimental data for the case of isothermal, creep foaming and produced qualitative trends under thermal cycling, superplastic conditions.

3. Pore clustering was modeled by changing the aspect ratio of the RVE, leading to an enhancement in foaming rates for both isothermal and cyclic foaming, which was more marked for the former conditions. Stress concentrations due to stress-field overlap during pore clustering are the cause of this enhancement. Another effect of pore clustering is anisotropic pore growth, causing the originally spherical pores to become elongated during growth.

4. The modeling of a bimodal distribution of pore sizes using a two-pore RVE led to predictions in foaming rate that are very similar to the predictions for a single pore size.

Acknowledgements

This research was supported by US National Science Foundation through Grant DMR-0108342/001. N.G.D.M. also thank the US Department of Defense for a NDSEG Fellowship, the Zonta Foundation for the Amelia Earhart Fellowship, and the American Association of University Women for a Selected Professions Dissertation Year Fellowship.

References

[1] Murray NGD, Dunand DC. Effect of thermal history on the superplastic expansion of argon-filled pores in titanium: Part I kinetics and microstructure. Acta Mater 2004, doi:10.1016/j.actamat.2004.01.039.
[2] Kearns MW, Blenkinsop PA, Barber AC, Farthing TW. Met Mater 1987;3:85.
[3] Kearns MW, Blenkinsop PA, Barber AC, Farthing TW. Int J Powder Metall 1988;24:59.
[4] Martin RL, Lederich RJ. Advances in Powder Metallurgy: Proceeding of the 1991 Powder Metallurgy Conference and Exposition, vol. 5. Powder Metallurgy Industries Federation, Princeton; 1991. p. 361.
[5] Queheillalt DT, Choi BW, Schwartz DS, Wadley HNG. Metall Mater Trans A 2000;31:261.
[6] Elzey DM, Wadley HNG. Acta Mater 2001;49:849.
[7] Queheillalt DT, Gable KA, Wadley HNG. Scr Mater 2001;44:409.
[8] Vancheeswaran R, Queheillalt DT, Elzey DM, Wadley HNG. Metall Mater Trans 2001;32:1813.
[9] Dunand DC, Teisen J. In: Schwartz DS, Shih DS, Wadley HNG, Evans AG, editors. Porous and cellular materials for structural applications, vol. 521. Pittsburgh: MRS; 1998. p. 231.
[10] Davis NG, Teisen J, Schuh C, Dunand DC. J Mater Res 2001;16:1508.
[11] Murray NGD, Schuh CA, Dunand DC. Scr Mater 2003;49:879.
[12] Murray NGD, Dunand DC. Compos Sci Technol 2003;63:2311.
[13] Dunand DC. In: Chandra T, Sakai T, editors. International Conference on Thermomechanical Processing of Steels and other Materials THERMEC'97. Warrendale, PA: TMS; 1997. p. 1821.
[14] Finnie L, Heller WR. Creep of engineering materials. New York: McGraw-Hill; 1959.
[15] Wilkinson DS, Ashby MF. Acta Metall 1975;23:1277.
[16] Wilkinson DS, Ashby MF. The development of pressure sintering maps. New York: Plenum Press; 1975. p. 473.
[17] Arzt E, Ashby MF, Easterling KE. Metall Trans A 1983;14:211.
[18] Duva JM, Crow PD. Acta Mater 1992;40:31.
[19] Helle AS, Easterling KE, Ashby MF. Acta Metall 1985;33:2163.
[20] Schuh C, Noel P, Dunand DC. Acta Mater 2000;48:1639.
[21] Parthasarathy TA, Shewmon PG. Metall Mater Trans A 1984;15:2021.
[22] Parthasarathy TA, Lopez HF, Shewmon PG. Metall Mater Trans A 1985;16:1143.
[23] Frost HJ, Ashby MF. Deformation-mechanism maps: the plasticity and creep of metals and ceramics. Oxford: Pergamon Press; 1982. 44.
[24] Nieh TG, Wadsworth J, Sherby OD. Superplasticity in metals and ceramics. Cambridge: Cambridge University Press; 1997.
[25] Greenwood GW, Johnson RH. Proc R Soc Lond A 1965;283:403.
[26] Schuh C, Dunand DC. Scr Mater 1999;40:1305.
[27] Frary M, Schuh C, Dunand DC. Metall Mater Trans A 2002;33:1669.
[28] Dunand DC, Myojin S. Mater Sci Eng A 1997;230:25.
[29] Dunand DC, Bedell CM. Acta Mater 1996;44:1063.
[30] Tvergaard V. Int J Fract 1981;17:389.
[31] Anderson PM, Rice JR. Acta Metall Mater 1985;1985:409.
[32] Mohan R, Brust FW. J Eng Mater Technol 2000;122:283.
[33] Li Z, Wang C, Chen C. Int J Solids Struct 2002;39:601.
[34] Hom CL, McMeeking RM. ASME J Appl Mech 1989;16:309.

[35] Worswick MJ, Pick PJ. J Mech Phys Solids 1990;38:601.
[36] Steenbrink AC, Van der Giessen E, Wu PD. J Mech Phys Solids 1997;45:405.
[37] Socrate S, Boyce MC. J Mech Phys Solids 2000;48:233.
[38] Christman T, Needleman A, Suresh S. Acta Metall 1989;37:3029.
[39] Tvergaard V. Acta Metall Mater 1990;38:185.
[40] Bao G, Hutchinson JW, McMeeking RM. Acta Metall Mater 1991;39:1871.
[41] Huang Y, Kinloch AJ. JOM 1992;27:2753.
[42] Hibbet K, Sorenson. ABAQUS Standard v 6.2, Providence, RI.
[43] Frary M, Schuh C, Dunand DC. Metall Mater Trans A 2002; 33:1669.
[44] Davis NG. Enhancement of solid-state foaming of titanium by transformation superplasticity. PhD thesis, Department of Materials Science and Engineering, Northwestern University, Evanston, IL; 2002.